# Topology Optimization of an Alternate Permanent Magnet Electrodynamic Suspension Using a 3-D Hybrid Analytical Model

Louis Beauloye, and Bruno Dehez
Institute of Mechanics, Materials, and Civil Engineering (iMMC), UCLouvain, Belgium

***Abstract*—This paper presents a novel gradient-based topology optimization method for the design of permanent magnet electrodynamic suspensions, using a 3-D hybrid analytical model. It enables the exploration of new magnet configurations, with the aim of improving both the lift-to-weight and lift-to-drag ratio. It reveals that a configuration with alternating poles in both the longitudinal and the transverse directions offers significantly better performance than the classical single-direction arrangement.**

## I. Introduction

Magnetic levitation (maglev) offers a promising solution for efficient and cleaner transportation. Among the possible suspension types for their levitation, electrodynamic suspensions (EDSs) are notable for their reliability and simplicity when built with permanent magnets (PMs) [1]. They rely on the interaction between these PMs attached to the vehicle and the currents they induce in a conductive track, producing two forces: a lift force in the levitation direction and a drag force opposite to the motion.

The PM configuration has a significant impact on the performance of the suspension system. To date, investigations have primarily focused on relatively simple configurations, including the Halbach array (HA) [2] and the alternation of magnetic poles (AltPM) [3], [4]. The former has the potential to generate higher forces, whereas the latter can be easier to construct.

Topology optimization (TO) is an optimal design approach that consists in finding the best way to distribute material in a given design domain [5]. This approach, applicable to electromagnetic problems, has already been applied to PM-EDS, but in 2-D, demonstrating the potential of the AltPM configuration [3]. New PM arrangements of PM-EDSs have also been investigated in 3-D with topology optimization based on a stochastic algorithm [4]. However, the number of optimization variables was limited due to the difficulty of achieving convergence in gradient-free TO [5]. The investigation of more complex PM-EDS topologies, considering the 3-D nature of the problem, would therefore require gradient-based TO approaches, and adapted models.

L. Beauloye is a Research Fellow of the Fonds de la Recherche Scientifique-FNRS

In that regard, finite element methods (FEM) are not appropriate because of the prohibitive computing time required to solve eddy current problems in 3-D. Similarly, magnetic equivalent circuits (MEC), which can also take advantage of their discrete nature to conduct a TO [6], would also be subject to long computation times for this type of problem. Nonetheless, the coupling of FEM or MEC, in certain regions of the problem, with Fourier modeling, in other regions, can be an ideal solution for carrying out TO in MEC regions. Such kind of hybrid analytical model (HAM) has been developed over the last few years to find the best compromise between model quality and efficiency [7].

In that context, the goal of this paper is therefore to investigate novel topologies of PM-EDS through a gradient-based TO using a 3-D hybrid analytical model. The combination of TO with such a kind of model has never been done to the author's best knowledge. Section II presents the HAM model. It is followed by the topology optimization problem, in Section III, including the sensitivities computation and the material interpolation scheme. The results are finally developed in Section IV.

## II. Hybrid analytical model

The optimizations carried out in this paper rely on a hybrid analytical model combining MEC and Fourier-based modeling. The following section describes this specific model and its application to TO. Only the important steps are presented and the focus is guided towards the TO.

### A. Description of the model

The model is applied to a geometry, illustrated in Fig. 1, divided into regions where different equations apply. A part of the domain (M) is discretized using MEC elements to be able to conduct a topology optimization whereas the rest is modeled using a mesh-free Fourier-based modeling to decrease the number of degrees of freedom but also capture eddy currents in a bulk conductive material.

*1) Assumptions:* The problem is made periodic along the $x$-axis and antiperiodic along the $y$-axis to be able to solve the equations in the Fourier regions. In the $x$-direction, the period of the model is equal to one full period on the

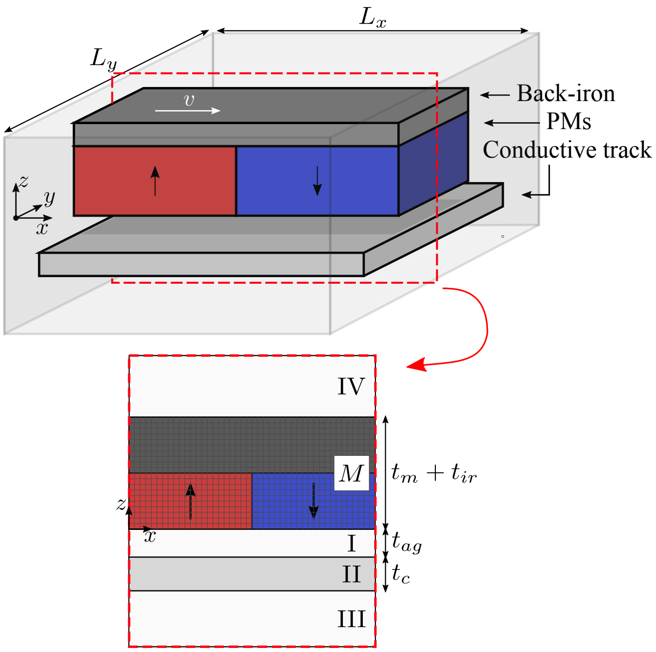


Fig. 1. Structure of the PM-EDS with the parameters and the division in regions.

magnetic field source. Doing so simplifies the analyses by neglecting the end-effects. In the other direction, the width of the model is equal to the width of the conductive plate. This condition coupled with the antiperiodicity condition in the $y$-direction allows for considering the finite width of the conductive plate. As long as the PM width is not too close to the width of the model, the side effects are taken into account. Considering the reference frame attached to the PMs, and steady-state conditions, the problem can be supposed quasi-static.

*2) MEC region:* In region M, a loop-formulation of the meshed MEC network is used [8], [9], meaning that it is based on the magnetic loop fluxes. The equations, analogous to Kirchoff's voltage law, therefore involve the loop fluxes $\varphi$, the reluctances $\mathcal{R}$, and the magnetomotive forces $\mathcal{F}$. These last two quantities can be computed from the physical properties and the dimensions of each MEC element along the three directions $x$, $y$, and $z$. All the loop equations can be assembled into the following system:

$$\boldsymbol{\mathcal{F}} = \boldsymbol{\Lambda}\boldsymbol{\mathcal{R}}\boldsymbol{\Lambda}^T\boldsymbol{\varphi} = \boldsymbol{\mathcal{L}}_{\mathcal{R}}\boldsymbol{\varphi} \tag{1}$$

where $\Lambda$ is an incidence matrix linking the loop fluxes to the branch fluxes inside each MEC element.

*3) Fourier region:* In regions I-IV, the following equations are solved [10], in the air:

$$\nabla^2\mathbf{A} = 0 \qquad \text{or} \qquad \nabla^2\Phi = 0 \tag{2}$$

and in the conductive material:

$$\nabla^2\mathbf{A} = \mu_0\sigma_c\left(\mathbf{v}\cdot\nabla\right)\mathbf{A} \tag{3}$$

where $\mathbf{A}$ is the magnetic vector potential, $\Phi$ is the magnetic scalar potential, $\sigma_c$ is the electrical conductivity, and $\mathbf{v}$ is the relative speed between the conductive track and the PMs. The general solution of such equations can be expressed as:

$$\Phi^{\mathrm{IV}} = \sum_{n=-N}^{N}\sum_{m=1}^{M}\left(C_{nm}^{\mathrm{IV}}e^{\alpha_{nm}z} + D_{nm}^{\mathrm{IV}}e^{-\alpha_{nm}z}\right) \times \sin\left(k_m y\right)e^{jk_n x} \tag{4}$$

$$A^{x,i} = \sum_{n=-N}^{N}\sum_{m=0}^{M}\left(C_{nm}^{x,i}e^{\gamma_{nm}z} + D_{nm}^{x,i}e^{-\gamma_{nm}z}\right) \times \cos\left(k_m y\right)\, e^{jk_n x} \tag{5}$$

$$A^{y,i} = \sum_{n=-N}^{N}\sum_{m=1}^{M}\left(C_{nm}^{y,i}e^{\gamma_{nm}z} + D_{nm}^{y,i}e^{-\gamma_{nm}z}\right) \times \sin\left(k_m y\right)\, e^{jk_n x} \tag{6}$$

with $i \in \{\mathrm{I}, \mathrm{II}, \mathrm{III}\}$, $N$, $M$ the numbers of harmonics in the $x$- and $y$-direction respectively, and

$$k_n = \frac{2n\pi}{L_x}, \qquad k_m = \frac{m\pi}{L_y}, \qquad \alpha_{nm} = \sqrt{k_n^2 + k_m^2} \tag{7}$$

$$\gamma_{nm} = \sqrt{\alpha_{nm}^2 + jk_n v_x \mu_0 \sigma_c \zeta_i} \tag{8}$$

$$\zeta_i = 1 \quad \text{if} \quad i = \mathrm{II}, \quad 0 \quad \text{otherwise} \tag{9}$$

They involve unknown coefficients $C$ and $D$ which can be found thanks to the boundary conditions between the regions. The following system of equations has therefore to be solved:

$$\boldsymbol{\mathcal{L}}_F\,\boldsymbol{\xi}^L = \mathbf{0} \tag{10}$$

where $\boldsymbol{\xi}^L$ is a vector containing all the unknown Fourier coefficients.

*4) Connection between Fourier and MEC regions:* The connection between the two types of regions requires special care since one is continuous and the other is discrete. However, the same boundary conditions still apply. The conservation of the normal component of the magnetic flux density is used to connect MEC to Fourier regions by expressing $B_z^M$ as a Fourier series. This translates into the following equations linking the loop fluxes to the Fourier coefficients:

$$\boldsymbol{\mathcal{B}}_F^U\,\boldsymbol{\xi}^U = \boldsymbol{\mathcal{B}}_M^{U\star}\,\boldsymbol{\varphi} \tag{11}$$

$$\boldsymbol{\mathcal{B}}_F^L\,\boldsymbol{\xi}^L = \boldsymbol{\mathcal{B}}_M^{L\star}\,\boldsymbol{\varphi} \tag{12}$$

The continuity of the tangential component of the magnetic field strength is ensured by expressing the Fourier region as an MMF source fed to the MEC region. The MEC system of equations can therefore be written as:

$$\boldsymbol{\mathcal{L}}_{\mathcal{R}}\,\boldsymbol{\varphi} + \boldsymbol{\mathcal{F}}_F^U\,\boldsymbol{\xi}^U - \boldsymbol{\mathcal{F}}_F^L\,\boldsymbol{\xi}^L = \boldsymbol{\mathcal{F}} \tag{13}$$

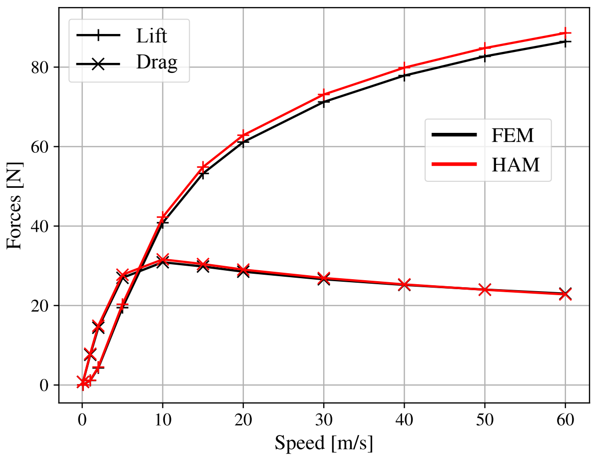


Fig. 2. Comparison of the forces computed with the HAM and FEM model for specific dimensions

*5) Global system:* All the equations can be assembled into the following linear system:

$$\mathbf{A}\mathbf{u} = \mathbf{b} \tag{14}$$

with

$$\mathbf{A} = \begin{bmatrix} \boldsymbol{\mathcal{L}}_{\mathcal{R}} & \boldsymbol{\mathcal{F}}_F^U & -\boldsymbol{\mathcal{F}}_F^L \\ \boldsymbol{\mathcal{B}}_M^{U\star} & -\boldsymbol{\mathcal{B}}_F^U & \mathbf{0} \\ \boldsymbol{\mathcal{B}}_M^{L\star} & \mathbf{0} & -\boldsymbol{\mathcal{B}}_F^L \\ \mathbf{0} & \mathbf{0} & \boldsymbol{\mathcal{L}}_F \end{bmatrix} \tag{15}$$

$$\mathbf{u} = \left[\boldsymbol{\varphi}^T \left(\boldsymbol{\xi}^U\right)^T \left(\boldsymbol{\xi}^L\right)^T\right]^T \tag{16}$$

$$\mathbf{b} = \left[\boldsymbol{\mathcal{F}}^T\, \mathbf{0}\, \mathbf{0}\, \mathbf{0}\right]^T \tag{17}$$

Once this system is solved, the forces can be computed from the integration of Maxwell's stress tensor on the surface of the conductive plate, at $z = -t_{ag}$. These forces have been compared to the ones computed in FEM using COMSOL Multiphysics for a specific set of dimensions. Fig. 2 shows a great agreement between the two as they evolve with the speed.

## III. Topology optimization

### A. Problem formulation

The goal is to perform a bi-objective optimization of the lift-to-drag (LDR) and lift-to-weight ratio (LWR), two common figures of merit of PM-EDS. However, as gradient-based TO approaches can only handle a single objective, the LWR is optimized while the LDR is used as a constraint in order to form a Pareto front point-by-point. The optimization problem can therefore be written as:

$$\begin{cases} \max\limits_{\boldsymbol{\rho}^+,\boldsymbol{\rho}^-} & \mathrm{LWR}(\mathbf{u}(\boldsymbol{\rho}^+,\boldsymbol{\rho}^-),\boldsymbol{\rho}^+,\boldsymbol{\rho}^-) \\ \text{s.t.} & \mathrm{LDR}(\mathbf{u}(\boldsymbol{\rho}^+,\boldsymbol{\rho}^-),\boldsymbol{\rho}^+,\boldsymbol{\rho}^-) \geq \mathrm{LDR}_{min} \\ & \rho_i^+ + \rho_i^- \leq 1 \quad \forall i \end{cases} \tag{18}$$

where $\rho_i^+$ (resp. $\rho_i^-$) is the z-positive (resp. z-neg.) magnetization density in the element $i$. These densities are linked to the remanent magnetic flux density $B_{r,i}$ inside each element $i$ by:

$$B_{r,i} = (\rho_i^+ - \rho_i^-)B_r \tag{19}$$

### B. Sensitivities computation

The sensitivity of the objective functions $F$ to the material densities is required. To do so, the Adjoint Variable Method (AVM) is used [5].

In this case, the sensitivities can be written as:

$$\frac{dF}{d\rho_i} = \frac{\partial F}{\partial \rho_i} + \boldsymbol{\lambda}^T \frac{\partial \mathbf{b}}{\partial \rho_i} \tag{20}$$

where $\boldsymbol{\lambda}$ is the adjoint variable, and is computed from the following adjoint system:

$$\mathbf{A}^T \boldsymbol{\lambda} = -\frac{\partial F}{\partial \mathbf{u}} \tag{21}$$

The proposed approach, based on a hybrid analytical model, is useful to compute the partial derivative of the objective and constraint function with respect to the state variables. The objectives and constraints considered here only involve the electromagnetic forces which depend only on the Fourier coefficients.

Since these coefficients are complex, the system has to be rewritten so that only real variables are used:

$$\mathbf{A} = \begin{bmatrix} \boldsymbol{\mathcal{L}}_{\mathcal{R}} & \boldsymbol{\mathcal{F}}_F^U & -\boldsymbol{\mathcal{F}}_F^L & j\boldsymbol{\mathcal{F}}_F^U & -j\boldsymbol{\mathcal{F}}_F^L \\ \mathrm{R}\left[\boldsymbol{\mathcal{B}}_M^{U\star}\right] & -\mathrm{R}\left[\boldsymbol{\mathcal{B}}_F^U\right] & \mathbf{0} & \mathrm{I}\left[\boldsymbol{\mathcal{B}}_F^U\right] & \mathbf{0} \\ \mathrm{I}\left[\boldsymbol{\mathcal{B}}_M^{U\star}\right] & -\mathrm{I}\left[\boldsymbol{\mathcal{B}}_F^U\right] & \mathbf{0} & -\mathrm{R}\left[\boldsymbol{\mathcal{B}}_F^U\right] & \mathbf{0} \\ \mathrm{R}\left[\boldsymbol{\mathcal{B}}_M^{L\star}\right] & \mathbf{0} & -\mathrm{R}\left[\boldsymbol{\mathcal{B}}_F^U\right] & \mathbf{0} & \mathrm{I}\left[\boldsymbol{\mathcal{B}}_F^U\right] \\ \mathrm{I}\left[\boldsymbol{\mathcal{B}}_M^{L\star}\right] & \mathbf{0} & -\mathrm{I}\left[\boldsymbol{\mathcal{B}}_F^U\right] & \mathbf{0} & -\mathrm{R}\left[\boldsymbol{\mathcal{B}}_F^U\right] \\ \mathbf{0} & \mathbf{0} & \mathrm{R}\left[\boldsymbol{\mathcal{L}}_F\right] & \mathbf{0} & -\mathrm{I}\left[\boldsymbol{\mathcal{L}}_F\right] \\ \mathbf{0} & \mathbf{0} & \mathrm{I}\left[\boldsymbol{\mathcal{L}}_F\right] & \mathbf{0} & \mathrm{R}\left[\boldsymbol{\mathcal{L}}_F\right] \end{bmatrix} \tag{22}$$

$$\mathbf{u} = \left[\boldsymbol{\varphi}^T \left(\boldsymbol{\xi}_R^U\right)^T \left(\boldsymbol{\xi}_R^L\right)^T \left(\boldsymbol{\xi}_I^U\right)^T \left(\boldsymbol{\xi}_I^L\right)^T\right]^T \tag{23}$$

$$\mathbf{b} = \left[\boldsymbol{\mathcal{F}}^T\, \mathbf{0}\, \mathbf{0}\, \mathbf{0}\, \mathbf{0}\, \mathbf{0}\right]^T \tag{24}$$

where $\mathrm{R}[\cdot]$ denotes the real part and $\mathrm{I}[\cdot]$ the imaginary part operators, $\xi_R$ and $\xi_I$ are the real and imaginary parts of the Fourier coefficients.

The drag and lift forces can be computed as:

$$F_d = \frac{1}{2\mu_0}\mathrm{Re}\int_x\int_y B_x \times \overline{B_z}\,dxdy \tag{25}$$

$$F_l = \frac{1}{4\mu_0}\mathrm{Re}\int_x\int_y (B_z \times \overline{B_z} - B_x \times \overline{B_x} - B_y \times \overline{B_y})dxdy \tag{26}$$

Each magnetic flux density has the following expression:

$$B_x = \sum_k (a_k(x,y) + jb_k(x,y))(\xi_{R,k}^L + j\xi_{I,k}^L) \tag{27}$$

$$B_y = \sum_k (r_k(x,y) + j s_k(x,y))(\xi^L_{R,k} + j\xi^L_{I,k}) \tag{28}$$

$$B_z = \sum_k (u_k(x,y) + j v_k(x,y))(\xi^L_{R,k} + j\xi^L_{I,k}) \tag{29}$$

with $a_k$, $b_k$, $r_k$, $s_k$, $u_k$, and $v_k$ real functions of $x$ and $y$. Injecting the expressions of the magnetic flux densities inside the forces and taking the derivative with respect to the Fourier coefficients, yields:

$$\frac{\partial F_d}{\partial \xi^L_{R,k}} = \frac{1}{2\mu_0}\int_x\int_y \Big(\mathrm{Re}\,(B_z)\,a_k + \mathrm{Im}\,(B_z)\,b_k + \mathrm{Re}\,(B_x)\,u_k + \mathrm{Im}\,(B_z)\,v_k\Big)dxdy \tag{30}$$

$$\frac{\partial F_d}{\partial \xi^L_{I,k}} = \frac{1}{2\mu_0}\int_x\int_y \Big(-\mathrm{Re}\,(B_z)\,b_k + \mathrm{Im}\,(B_z)\,a_k - \mathrm{Re}\,(B_x)\,v_k + \mathrm{Im}\,(B_z)\,u_k\Big)dxdy \tag{31}$$

$$\frac{\partial F_l}{\partial \xi^L_{R,k}} = \frac{1}{4\mu_0}\int_x\int_y 2\Big(\mathrm{Re}\,(B_z)\,u_k + \mathrm{Im}\,(B_z)\,v_k - \mathrm{Re}\,(B_x)\,a_k - \mathrm{Im}\,(B_z)\,b_k - \mathrm{Re}\,(B_y)\,r_k - \mathrm{Im}\,(B_y)\,s_k\Big)dxdy \tag{32}$$

$$\frac{\partial F_l}{\partial \xi^L_{I,k}} = \frac{1}{4\mu_0}\int_x\int_y 2\Big(-\mathrm{Re}\,(B_z)\,v_k + \mathrm{Im}\,(B_z)\,u_k + \mathrm{Re}\,(B_x)\,b_k - \mathrm{Im}\,(B_z)\,a_k + \mathrm{Re}\,(B_y)\,s_k - \mathrm{Im}\,(B_y)\,r_k\Big)dxdy \tag{33}$$

These derivatives are used to compute the derivative of the objective and constraint functions:

$$\frac{\partial \mathrm{LWR}}{\partial \xi^L_k} = \frac{1}{W}\frac{\partial F_l}{\partial \xi^L_k} \tag{34}$$

$$\frac{\partial \mathrm{LDR}}{\partial \xi^L_k} = \frac{\frac{\partial F_l}{\partial \xi^L_k}F_d - F_l\frac{\partial F_d}{\partial \xi^L_k}}{F_d^2} \tag{35}$$

with $W$ the PM weight.

### C. Optimization

The optimization is carried out with the Method of Moving Asymptotes (MMA) algorithm [11] implemented using [12]. To reduce the computation time, the optimization variables are defined in the $xy$-plane on half the period. 12 by 12 elements are used in the design space, shown in Fig. 3. The result is then extruded along the z-axis and replicated with an opposite sign on the other half of the period. The sensitivities are adapted accordingly. The parameters of the PM-EDS employed in the optimization process are detailed in Table I.

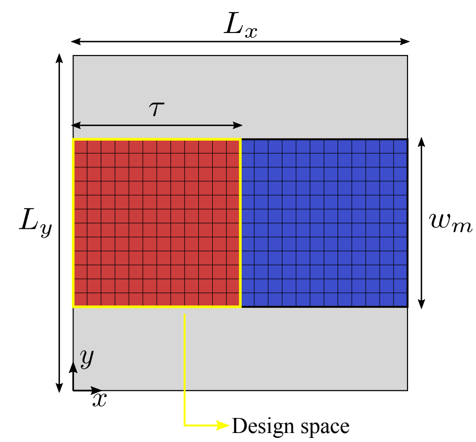


Fig. 3. Illustration of the design space in the $xy$-plane

TABLE I
PM-EDS PARAMETERS

| Parameter | Symbol | Value | Unit |
|---|---|---|---|
| Air gap thickness | $t_{ag}$ | 30 | mm |
| PM thickness | $t_m$ | $\{50,\ 100\}$ | mm |
| Domain pole pitch | $\tau$ | $\{60,\ 120\}$ | mm |
| PM width | $w_m$ | $\{60,\ 120\}$ | mm |
| Back-iron thickness | $t_{ir}$ | 10 | mm |
| PM remanence | $B_r$ | 1.4 | T |
| Track thickness | $t_c$ | 30 | mm |
| Track conductivity | $\sigma_c$ | 3.5e7 | S/m |
| Track width | $L_y$ | $3\tau$ | mm |
| Track length | $L_x$ | $2\tau$ | mm |
| Back-iron permeability | $\mu_{r,ir}$ | 1000 | - |
| Translational speed | $v_x$ | 50 | m/s |

### D. Material Interpolation Scheme

A simple linear relation between the remanent magnetic flux density and the material density inside each element can be used. However, as shown below, even if this interpolation scheme naturally converges to topologies with no mixed material, it is prone to be trapped in local minima. To overcome this issue, the following modified interpolation scheme can be used:

$$\rho^*_\alpha = \frac{1-r_\alpha}{1-r_\alpha\rho_\alpha}\rho_\alpha \tag{36}$$

where $r_\alpha$ is a coefficient that can be varied between a negative value to promote mixed materials and 0 to fall back on the simple linear interpolation scheme [13]. The topology optimization is first conducted with $r_\alpha = -10$. The results are then reevaluated with all the densities forced to be equal to 0 or 1.

A Pareto front obtained after the optimization is shown in Fig. 4, before and after reevaluation. The gray points on the graph correspond to topologies that do not belong to the global Pareto front after reevaluation. As illustrated with the

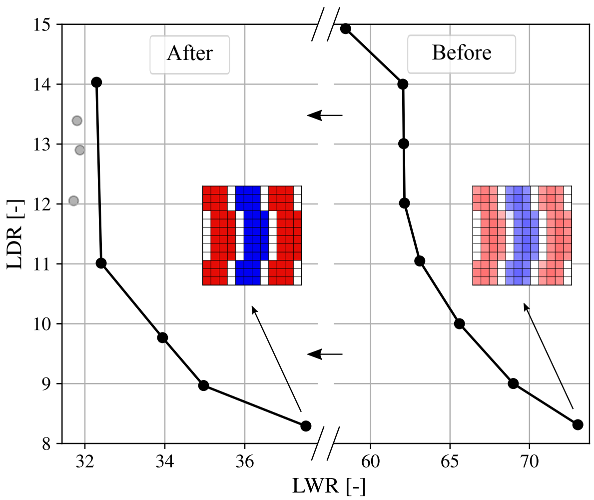


Fig. 4. A result of the topology optimization before and after reevaluation with the densities forced to 0 or 1.

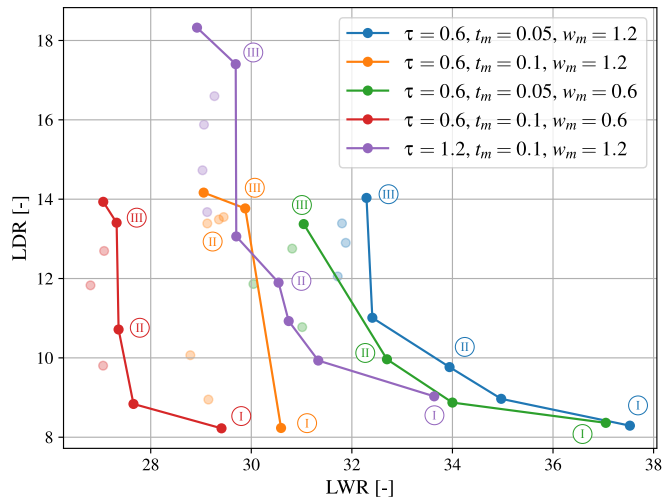


Fig. 6. Topology optimization results for five different sets of dimensions. The numbers indicate different kinds of topology.

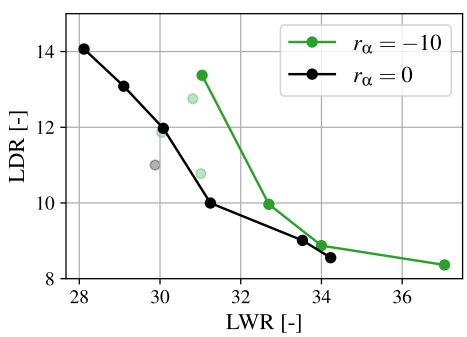


Fig. 5. Comparison between a topology optimization conducted with the linear material interpolation scheme in black and with the proposed one in green.

example topology shown in Fig. 4, the first optimization step gives rise to a blurry solution, revealing that the optimization finds a trade-off between a high remanent flux density and a low weight, through intermediate densities. After reevaluation, the values of LWR are different since the densities have changed but the relative position of the points stayed almost the same. The LDR values are also approximately constant because this objective is only slightly dependent on the $B_r$. These last two observations justify a posteriori the choice of optimizing the LWR while using the LDR as a constraint and not the other way around.

Fig. 5 shows a comparison between the results of an optimization conducted using $r_\alpha = 0$, on the one hand, and using $r_\alpha = -10$ after reevaluation, on the other hand. It highlights that a two-step optimization strategy, implementing a material-promoting interpolation scheme, achieves better results. Besides, for an LDR equal to 11, the optimization conducted with $r_\alpha = 0$ falls into a local optimum.

## IV. Results

Several topology optimizations were conducted with five different sets of domain dimensions to explore a maximum number of topologies. The results are shown in Fig. 6.

The best Pareto front is obtained for a domain pole pitch $\tau$ of 0.6 m, a larger width $w_m$, and a smaller PM thickness $t_m$. Decreasing the width or increasing the PM thickness has a negative effect on the LWR. Since the LDR is proportional to the square root of the pole pitch, a larger domain pole pitch $\tau$ can lead to a larger effective PM pole pitch and therefore a higher LDR.

Some of the topologies behind the fronts are referenced by a number and a color, and then represented in Fig. 7. All the topologies with the highest LWR and lowest LDR (I) are equivalent to the classical alternate permanent magnet topology with a specific pole pitch around 0.2 m. At the other side of the fronts (III), we can also find alternating poles but in both $x$- and $y$-directions, and with a higher pole pitch. This is in line with a previous study conducted in [4] but with a different approach. In between (II), some original and quite unexpected PM arrangements emerge with mixed performance.

It can be noticed that the optimization struggles more to converge with the 1.2m pole pitch, probably because it is harder to create the optimum pole pitch with the same number of elements on a longer domain.

To assess the optimality of the new topology (III), the classical topology (I) was evaluated with a longer pole pitch. In Table II, the performance of both topologies, evaluated with the HAM model, is compared with the maximum pole pitch and the two PM thicknesses. The new doubly alternate configuration clearly outperforms the classical topology with a significantly higher LWR and a similar LDR.

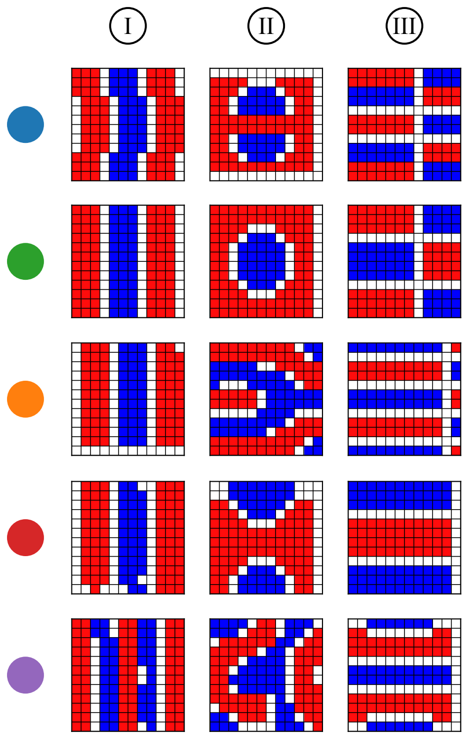


Fig. 7. Topologies found on the Pareto fronts. The colors and the number indicate respectively the front and the position of the topology on the front. Only one pole pitch is represented with its 12x12 grid on which the optimization is performed.

TABLE II
COMPARISON OF THE PERFORMANCE OF THE ORIGINAL AND THE CLASSICAL TOPOLOGIES

| | 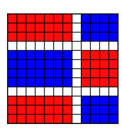 | | 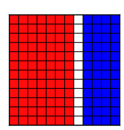 | |
|---|---|---|---|---|
| $t_m$ [mm] | 50 | 100 | 50 | 100 |
| LDR [-] | 14 | 13.4 | 12.3 | 13.2 |
| LWR [-] | 32.3 | 27.3 | 16.3 | 20.6 |

## V. CONCLUSION

This paper presented a gradient-based topology optimization method relying on hybrid analytical models. Applied to the optimization of the permanent magnet arrangement of electrodynamic suspensions, it proved to be effective in dealing with complex 3-D electromagnetic problems.

More specifically, regarding the method, it showed how a hybrid analytical model can be adapted and used for topology optimization purposes making the MEC region of the HAM model coincide with the design region of the topology optimization.

Regarding the application, the topology optimization yielded different topologies using a dedicated scheme to avoid local minima. It was found that an original double alternate topology, with alternating magnetic poles in both $x$- and $y$-directions, can significantly increase the lift-to-weight ratio of the suspension for the same lift-to-drag ratio compared to the simple alternating poles. The next step is to parameterize both topologies and optimize them when integrated into a real application including dimensional and operational constraints.

## REFERENCES

[1] L. Beauloye and B. Dehez, "Permanent Magnet Electrodynamic Suspensions Applied to MAGLEV Transportation Systems: A Review," *IEEE Transactions on Transportation Electrification*, vol. 9, no. 1, pp. 748–758, Mar. 2023.

[2] Z. Deng, H. Shi, Z. Ke, J. Liu, Z. Li, B. Zhang, Z. Jiang, J. Zhou, and Y. Liu, "Permanent magnet electrodynamic suspension system integrated with a car: Design, implementation, and test," *IEEE Transactions on Transportation Electrification*, vol. 10, no. 1, pp. 1101–1115, 2024.

[3] L. Beauloye and B. Dehez, "Impact of the Magnet Span on the Forces of Electrodynamic Suspensions with an Alternate Permanent Magnet Arrangement," in *2022 25th International Conference on Electrical Machines and Systems (ICEMS)*. Chiang Mai, Thailand: IEEE, Nov. 2022, pp. 1–5.

[4] ——, "Topology optimization of an alternate permanent magnet electrodynamic suspension," in *2023 IEEE Energy Conversion Congress and Exposition (ECCE)*, 2023, pp. 4532–4537.

[5] F. Lucchini, R. Torchio, V. Cirimele, P. Alotto, and P. Bettini, "Topology optimization for electromagnetics: A survey," *IEEE Access*, vol. 10, p. 98593–98611, 2022.

[6] M. Yin, M. Naidjate, N. Bracikowski, A. Pierquin, and D. Trichet, "Topology optimization of non-linear electromagnetic actuator based on reluctance network analysis," *Journal of Magnetism and Magnetic Materials*, vol. 602, p. 172174, Jul. 2024.

[7] K. J. W. Pluk, J. W. Jansen, and E. A. Lomonova, "3-d hybrid analytical modeling: 3-d fourier modeling combined with mesh-based 3-d magnetic equivalent circuits," *IEEE Transactions on Magnetics*, vol. 51, no. 12, p. 1–14, Dec. 2015.

[8] N. Verbeek, F. Baudart, and B. Dehez, "Loop formulation in hybrid analytical modeling for solving 2-d nonlinear magnetostatic problems," *IEEE Transactions on Magnetics*, vol. 57, no. 8, p. 1–9, Aug. 2021.

[9] Y. Benmessaoud, F. Dubas, R. Beniamineand, and M. Hilairet, "Three-dimensional automatic generation magnetic equivalent circuit using mesh-based formulation," in *2017 20th International Conference on Electrical Machines and Systems (ICEMS)*. Sydney, Australia: IEEE, Aug. 2017, p. 1–6.

[10] S. Paul and J. Z. Bird, "A 3-d analytic eddy current model for a finite width conductive plate," *COMPEL*, vol. 33, no. 1/2, p. 688–706, Dec. 2013.

[11] K. Svanberg, "The method of moving asymptotes—a new method for structural optimization," *International Journal for Numerical Methods in Engineering*, vol. 24, no. 2, pp. 359–373, 1987.

[12] A. Deetman, "GCMMA-MMA-Python: Python implementation of the Method of Moving Asymptotes," Aug. 2024. [Online]. Available: https://doi.org/10.5281/zenodo.13337495

[13] T. Labbe and B. Dehez, "Convexity-oriented mapping method for the topology optimization of electromagnetic devices composed of iron and coils," *IEEE Transactions on Magnetics*, vol. 46, no. 5, p. 1177–1185, May 2010.